INTERNATIONAL JOURNAL FOR NUMERICAL METHODS IN ENGINEERING
Int. J. Numer. Meth. Engng (in press)
Published online in Wiley InterScience (www.interscience.wiley.com). DOI: 10.1002/nme.1598

Spatial convergence of crack nucleation using a cohesive finite-element model on a pinwheel-based mesh

Katerina D. Papoulia[1,*,†], Stephen A. Vavasis[2,‡] and Pritam Ganguly[3,§]

[1]*School of Civil and Environmental Engineering, Cornell University, Ithaca, NY 14853, U.S.A.*
[2]*Department of Computer Science, Cornell University, Ithaca, NY 14853, U.S.A.*
[3]*Department of Theoretical and Applied Mechanics, Cornell University, Ithaca, NY 14853, U.S.A.*

SUMMARY

We consider the use of initially rigid cohesive interface models in a two-dimensional dynamic finite-element solution of a fracture process. Our focus is on convergence of finite-element solutions to a solution of the undiscretized medium as the mesh spacing Δx (and therefore time-step Δt) tends to zero. We propose the use of pinwheel meshes, which possess the 'isoperimetric property' that for any curve C in the computational domain, there is an approximation to C using mesh edges that tends to C including a correct representation of its length, as the grid size tends to zero. We suggest that the isoperimetric property is a necessary condition for any possible spatial convergence proof in the general case that the crack path is not known in advance. Conversely, we establish that if the pinwheel mesh is used, the discrete interface first activated in the finite-element model will converge to the initial crack in the undiscretized medium. Finally, we carry out a mesh refinement experiment to check convergence of both nucleation and propagation. Our results indicate that the crack path computed in the pinwheel mesh is more stable as the mesh is refined compared to other types of meshes. Copyright © 2006 John Wiley & Sons, Ltd.

KEY WORDS: cohesive zone modelling; finite element; convergence; crack nucleation; mesh dependence

1. RIGID COHESIVE MODELS

Cohesive zone modelling, which was originally proposed by Dugdale [1], Barenblatt [2] and Rice [3], represents cracks as displacement discontinuities in a solid body. The separation of

*Correspondence to: Katerina D. Papoulia, School of Civil and Environmental Engineering, Cornell University, Ithaca, NY 14853, U.S.A.
†E-mail: kp58@cornell.edu
‡E-mail: vavasis@cs.cornell.edu
§E-mail: pg45@cornell.edu

Contract/grant sponsor: NSF CAREER award; contract/grant number: CMS-0239068
Contract/grant sponsor: NSF; contract/grant number: CMS-0220327
Contract/grant sponsor: NSF; contract/grant number: CCF-0085969

Received 11 June 2005
Revised 4 October 2005
Accepted 21 October 2005

bulk material across the crack is resisted by cohesive tractions, governed by the corresponding cohesive constitutive model. The cohesive tractions are usually taken to be a function of the opening displacement of the interface.

The most straightforward application of cohesive modelling is to problems where predefined interfaces exist [4–15]. In such analyses, the fracture path is assumed *a priori* and can usually be justified by the nature of the problem (e.g. physical weak interfaces in delamination problems) or by experimental data. Cohesive interface elements are prepositioned along the specified crack path.

On the other hand, for applications in which the crack path is not known in advance [16–20], cohesive interface elements must be placed along the path *a posteriori* as it opens, and the path must be determined as part of the solution of the governing equations. Generally, this requires some kind of adaptive approach, in which cohesive surfaces are activated only as needed.

Three kinds of adaptive methods are prominent in the literature: remeshing every time-step at the tip of the crack thereby adapting the mesh [21], adaptively enriching finite-element basis functions to represent displacement discontinuities [22], or adaptively inserting (also called 'activating') cohesive elements on the boundaries of existing volume elements [17, 23], which is the focus of this paper. It is typical in the latter approach to consider every single element boundary as a potential cohesive interface site. Both remeshing and enriched basis functions entail additional complexity in the computational methods as well as new issues concerning the validity of the numerical modelling (e.g. criteria for direction of propagation and issues of transferring state variable information).

A major advantage of adaptive approaches is that the effective initial stiffness of the cohesive model (prior to activation) is infinite, and therefore the inactive cohesive interfaces have no effect on the bulk elastic properties [24]. We call this type of model *initially rigid* or simply *rigid* [25] (also called extrinsic [26]).

2. REPRESENTING THE CRACK PATH IN THE MESH

As explained in the previous section, in this paper it is assumed that the crack path in the finite-element model is composed of activated interfaces all of which lie on boundaries of finite elements in the initial mesh. The crack path in the undiscretized medium, henceforth called the 'mathematical crack path', on the other hand, has no such constraint. This discrepancy has been noted by other authors, and indeed has led some to propose new classes of cohesive fracture models that represent cracks as collections of disconnected line segments [27] or using particle-based discretization [28]. Enriched basis function techniques have also been extended to dynamic cohesive fracture, including branching cracks [29]. Although these classes of methods are able to solve the crack discrepancy problem, they introduce new issues because they give up some of the advantages of traditional finite elements.

To analyse the impact of this discrepancy, we first consider the sense in which a discrete crack representation can converge to the mathematical path. One simple approach would use the classical Hausdorff distance, which states that the distance from curve A to curve B, both lying in the same two-dimensional domain, is the maximum over $\mathbf{a} \in A$ of the distance from $\mathbf{a}$ to the closest $\mathbf{b} \in B$. Convergence in the Hausdorff sense, however, does not guarantee convergence of the length: a sequence of paths $P_1, P_2, \ldots$ can converge to a path P while the sequence $\text{length}(P_1), \text{length}(P_2), \ldots$ converges to a quantity strictly greater than $\text{length}(P)$. An example

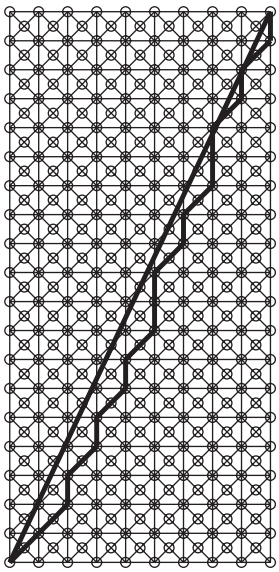

Figure 1. If the mathematical crack path is the line segment connecting the extreme corners of this cross-quadrilateral mesh, then the best approximation to it (which is not uniquely determined) using mesh edges is the jagged path indicated. No matter how much the mesh is refined, the jagged path will always be approximately 8% longer than the mathematical path.

like this is not pathological; indeed, failure of length to converge is the typical behaviour for any family of structured meshes. For example, consider the standard cross-quadrilateral mesh family with aspect ratio 1 : 1. This mesh is formed by dividing the computational domain into equally sized axis-parallel squares and then dividing each square with two diagonal cuts into four triangles. Let P be a line segment in the computational domain and let $P_1, P_2, \ldots$ be the closest approximations to P in a sequence of cross-quadrilateral meshes of the domain whose mesh size tends to zero. It is not hard to see that unless the orientation of P with respect to the x-axis is 0, 45, 90 or 135°, the sequence $\text{length}(P_1)$, $\text{length}(P_2), \ldots$, does not converge to $\text{length}(P)$ (see Figure 1).

The length of the discrete versus mathematical crack path is significant physically because a fundamental assumption for most cohesive models is that the energy needed to create a crack is proportional to its length. This leads us to conjecture that a necessary condition for spatial convergence in cohesive modelling is that the sequence of meshes $\mathscr{M}_1, \mathscr{M}_2, \ldots$ must contain a sequence of paths $P_1, P_2, \ldots$ such that $P_i \to P$ in the Hausdorff sense and such that $\text{length}(P_i) \to \text{length}(P)$, where P is the mathematical crack solution.

Evidence for this conjecture arises from computational experiments as well. For example, Sam [30] modelled the laboratory experiment due to Kalthoff and Winkler [31] in which a plate of high-strength steel with two edge notches was impacted by a steel projectile. The laboratory experiment showed that the crack propagated at an angle of about 70° from one of the notches with respect to the notch. Sam used cross-triangle quadrilateral meshes in which the aspect ratio of the quadrilaterals were varied. The point of varying the aspect ratio was to

make the diagonals of the quadrilaterals either closely aligned or not so closely aligned with the 70° direction. He found that the crack path depended significantly on the aspect ratio. In meshes with diagonals close to 70°, the crack generally followed one of the available diagonal paths. In meshes with no diagonals close to 70°, the crack zigzagged substantially. (Zhang and Paulino [32] reported results on the Kalthoff experiment that were less mesh dependent.)

3. PINWHEEL MESHES

As mentioned earlier, the goal of rigid cohesive modelling is often to solve problems in which the crack path is not known in advance but is an outcome of the simulation. Based on the results in the previous section, we conclude that if spatial convergence is desired, the family of meshes must represent every possible crack path both in the Hausdorff sense and in the sense of length. There is one family of meshes known to have this property, namely, pinwheel meshes in two dimensions. The pinwheel mesh is derived from Radin and Conway's [33] pinwheel tiling, which we now describe. The pinwheel tiling starts with a $1:2:\sqrt{5}$ right triangle T_0 and subdivides it into five $1:2:\sqrt{5}$ subtriangles that are similar to each other, see Figure 2(a). This subdivision process may be repeated indefinitely, yielding a tiling of the original triangle with an arbitrary level of refinement. The distinction between a tiling and a mesh is that the triangles in a tiling are not required to meet edge-to-edge and therefore may have hanging nodes. To change the tiling into a triangulation, one splits all the $1:2:\sqrt{5}$ triangles at the final recursion level of the tiling into three as shown in Figure 2(b) by bisecting their hypotenuse and longer leg. This creates new nodes and causes all triangles to meet simplicially (edge-to-edge).

Radin and Sadun [34] have proved that the pinwheel tiling has the following *isoperimetric property*. Let $\mathscr{M}_1, \mathscr{M}_2, \ldots$ be the sequence of pinwheel tilings such that $\mathscr{M}_i$ repeats the construction in the previous paragraph to the ith level (and thus contains 5^i tiles). Let L be an arbitrary line segment in the initial triangle T_0. Then the 1-skeleton (i.e. union of tile edges) of $\mathscr{M}_i$ contains a path L_i such that the L_i's converge to L in the Hausdorff and length sense. Their theorem extends easily to arbitrary curves, since any curve can be approximated in the two senses by a path of line segments, and then the line segments can be approximated by the 1-skeleton of the mesh.

In recent work [35], we generalized the pinwheel tiling to arbitrary triangles (not only $1:2:\sqrt{5}$) and showed how to use this generalization to develop a mesh generator called PINW

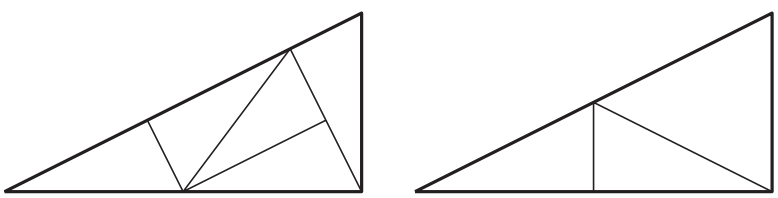

Figure 2. (a) The basic recursive pinwheel subdivision of a 1:2:$\sqrt{5}$ right triangle; and (b) subdividing a triangle at the final recursion level into three subtriangles to eliminate hanging nodes.

for arbitrary two-dimensional polygonal domains. The meshes produced by PINW possess the isoperimetric property.

4. STATEMENT OF THE MAIN RESULT

In this section, we state the main theoretical result of this paper. Its proof is in the next section. We first describe our assumptions about the mathematical problem, and then we describe our assumptions about the finite-element method. The setting is as follows. Let $\mathscr{B}$ be a two-dimensional body with piecewise smooth boundaries and no cusps or cracks. Let the initial displacements within the body be denoted $\mathbf{u}_0(\mathbf{x})$ and the initial velocities $\mathbf{v}_0(\mathbf{x})$, where $\mathbf{u}_0$ and $\mathbf{v}_0$ are given vector functions. Assume the body is subject to given time-varying continuous displacement boundary conditions $\Delta(\mathbf{x}, t)$ for $\mathbf{x} \in \Gamma_1$ and given time-varying traction boundary conditions $\bar{\tau}(\mathbf{x}, t)$ for $\mathbf{x} \in \Gamma_2$, where Γ_1, Γ_2 form a partition of $\partial\mathscr{B}$. Suppose the body is also subject to body forces $f(\mathbf{x}, t)$. The subsequent motion of the body is driven by these loads and is determined by plane-stress isotropic linear elasticity with Young's modulus E and Poisson ratio ν. Let $\bar{\mathscr{B}}$ be the closure of $\mathscr{B}$, i.e. $\bar{\mathscr{B}} = \mathscr{B} \cup \partial\mathscr{B}$. We assume that boundary and initial conditions and loads are sufficiently smooth so that $\boldsymbol{\sigma}(\mathbf{x}, t)$, the Cauchy stress, is a C^1 function of both space and time until the time of crack nucleation.

Assume that a crack nucleates in the body at time t^*, where $t^* > 0$, and spatial coordinate $\mathbf{x}^* \in \bar{\mathscr{B}}$. Assume that crack nucleation occurs when a criterion of the form $\lambda_{\max}(\boldsymbol{\sigma}(\mathbf{x}, t)) \geqslant \sigma_c$, where $\lambda_{\max}$ denotes the maximum eigenvalue of a tensor and σ_c is the critical traction for the material. Assume also that the orientation of the initial crack is orthogonal to the maximum normal stress. Denote the angle with respect to the x-axis of the normal to the initial crack as θ^*. That implies that $(\cos\theta^*, \sin\theta^*)$ is eigenvector of $\boldsymbol{\sigma}(\mathbf{x}^*, t^*)$ whose eigenvalue is σ_c. Let $h(\boldsymbol{\sigma}, \theta)$, where $\boldsymbol{\sigma}$ is a 2×2 symmetric tensor and θ is an angle, be defined as $(\cos\theta, \sin\theta)^{\mathrm{T}} \boldsymbol{\sigma} (\cos\theta, \sin\theta)$. Then equivalently we could say that the criterion is first satisfied when $h(\boldsymbol{\sigma}(\mathbf{x}^*, t^*), \theta^*) \geqslant \sigma_c$.

For the rest of this section and the next, we assume that the angle θ^* is understood $\bmod \pi$ to avoid specifying the sign of the eigenvector $(\cos\theta^*, \sin\theta^*)$. We let $\mathscr{A}$ denote the set of all angles taken $\bmod \pi$, and we define the distance $\mathrm{dist}_{\mathscr{A}}(\theta, \theta')$ between two angles to be the absolute difference between them, $\bmod \pi$. Thus, for $\theta \in \mathscr{A}$, $\cos\theta$ and $\sin\theta$ are not uniquely determined (since the signs are unknown) and yet the function $h(\boldsymbol{\sigma}, \theta)$ is well determined and continuously depends on both $\boldsymbol{\sigma}$ and θ.

To ensure that $(\mathbf{x}^*, t^*, \theta^*)$ is well-defined, we assume that the only solution $(\mathbf{x}, t, \theta)$ to the inequality $h(\sigma(\mathbf{x}, t), \theta) \geqslant \sigma_c$ lying in the set $\bar{\mathscr{B}} \times [0, t^*] \times \mathscr{A}$ is the single point $(\mathbf{x}^*, t^*, \theta^*)$.

Finally, we assume that

$$\left.\frac{\mathrm{d}h(\boldsymbol{\sigma}(\mathbf{x}^*, t), \theta^*)}{\mathrm{d}t}\right|_{(t^*)^-} > 0$$

to prevent a pathological situation in which $h(\boldsymbol{\sigma}(\mathbf{x}^*, t^*), \theta^*)$ attains the value σ_c but h immediately starts to decrease again. The notation $\mathrm{d}/\mathrm{d}t|_{(t^*)^-}$ means the left-derivative with respect to t evaluated at t^*.

Suppose that this problem is discretized with a linear elastic finite-element method in which initially rigid cohesive interface edge elements are placed between all the area elements. In order to show convergence as the spatial mesh is refined, we need to postulate the existence of

an infinite sequence of triangular meshes $\mathscr{M}_1, \mathscr{M}_2, \ldots$ of $\mathscr{B}$. Let h_i be the maximum diameter among triangles in mesh $\mathscr{M}_i$. We assume that $\lim_{i\to\infty} h_i = 0$.

We assume that the interface elements are activated when the normal component of traction evaluated at the midpoint of the interface exceeds σ_c. (The assumption of the midpoint is made for simplicity and is not crucial to our analysis.) There are several ways to evaluate this normal traction (see, e.g. Reference [36]). We allow any such method to be used as long as the following convergence property holds. As the mesh is refined, the computed value of the normal component of the traction on an interface whose normal is $\mathbf{n}$ should tend to $\boldsymbol{\sigma}\mathbf{n}$, where $\boldsymbol{\sigma}$ is the stress evaluated on either adjacent bulk element at the interface point. (Note that common finite-element discretizations possess jump discontinuities in $\boldsymbol{\sigma}$ at element boundaries. For such discretizations, it would be impossible to require that $\boldsymbol{\sigma}\mathbf{n}$ evaluated from the bulk element at the interface point be equal to the interface traction, since this value would be inconsistent with the value of $\boldsymbol{\sigma}\mathbf{n}$ computed from the other bulk element. So therefore, we require agreement only in the limit of $h_i \to 0$.)

In addition to assuming that $h_i \to 0$, we also assume that the meshes are *quasi-uniform*, which has the following definition. For $i = 1, 2, \ldots$, let $\rho_i = \min\{\text{inradius}(T) : T \in \mathscr{M}_i\}$. Quasi-uniformity means that for all i, $h_i/\rho_i \leqslant K$, where K is a fixed constant. This assumption has two implications. First, it implies that every triangle in every mesh is well-shaped, i.e. no triangle has a very small angle. Second, it implies that the degree of nonuniformity in the meshes does not increase as the mesh is refined, i.e. for each i, all the elements in $\mathscr{M}_i$ are roughly the same size. This assumption is commonplace in proofs of convergence.

An uncommon assumption, but one that is necessary for our analysis, is that as $i \to \infty$, for every point $\mathbf{x} \in \bar{\mathscr{B}}$ and every direction $\theta \in \mathscr{A}$, $\mathscr{M}_i$ has an edge arbitrarily close to $\mathbf{x}$ aligned arbitrarily close to θ. It is clear that some assumption like this must be necessary if we want to show that the first cohesive interface to nucleate is aligned in the correct orientation. We state this property of the sequence of meshes formally as follows. For every $\varepsilon > 0$, there exists an I such that for all $\mathbf{x} \in \bar{\mathscr{B}}$, all $\theta \in \mathscr{A}$ and all $i \geqslant I$, mesh $\mathscr{M}_i$ contains a triangle edge e such that $\text{dist}(\mathbf{x}, e) \leqslant \varepsilon$ and $\text{dist}_{\mathscr{A}}(\theta, \theta_e) \leqslant \varepsilon$. Let us call this property 'Property P'. We know of only one family of meshes with the three properties enumerated here (mesh diameter tends to zero, quasi-uniform and Property P), namely, the pinwheel family described in Section 3.

The finite-element method includes a time-stepping method. We assume that the time-step Δt_i used for mesh $\mathscr{M}_i$ is chosen sufficiently small so that convergence of the method is assured for the linear elastic bulk model, and specifically, $\lim_{i\to\infty} \Delta t_i = 0$. If explicit time-stepping is used, then the time-step must satisfy the CFL stability condition.

Now finally, we can state the consequence of all these assumptions. For the finite-element method on mesh $\mathscr{M}_i$, let the first interface to be activated be edge e_i, let its midpoint be $\mathbf{x}_i$ and its normal angle be θ_i. Let the time of its activation be t_i. Then as $i \to \infty$, $\mathbf{x}_i \to \mathbf{x}^*$, $t_i \to t^*$, and $\text{dist}_{\mathscr{A}}(\theta_i, \theta^*) \to 0$.

The proof of this result is given in the next section.

5. PROOF OF THE MAIN RESULT

In this section, we provide the proof that $(\mathbf{x}_i, t_i, \theta_i) \to (\mathbf{x}^*, t^*, \theta^*)$ as $i \to \infty$. Suppose we are given an $\varepsilon > 0$. The task of this section is to show how to select an I such that $\|\mathbf{x}_i - \mathbf{x}^*\| \leqslant \varepsilon$, $|t_i - t^*| \leqslant \varepsilon$ and $\text{dist}_{\mathscr{A}}(\theta_i, \theta^*) \leqslant \varepsilon$ for all $i \geqslant I$.

The proof uses primarily compactness arguments. Compactness arguments have been used before for proving convergence of numerical methods, e.g. the Lax-Wendroff theorem for hyperbolic conservation laws [37].

The following simple topological lemma is crucial to our proof.

Lemma 1

Let $g : C \to \mathbf{R}$ be a continuous function, where C is a compact set with a metric. Let a be a scalar, and suppose that the set $U = \{w \in C : g(w) \geqslant a\}$ is nonempty. Then for every $\varepsilon > 0$, there exists a $\delta > 0$ such that the set $V = \{w \in C : g(w) \geqslant a - \delta\}$ is contained in an open ε-neighbourhood of U.

Proof

Suppose not; then there exists an $\varepsilon > 0$ and a sequence $\delta_1, \delta_2, \ldots$ of positive numbers tending to zero such that for each i, there is a $w_i \in C$ satisfying $g(w_i) \geqslant a - \delta_i$ and $\text{dist}(w_i, U) \geqslant \varepsilon$. Since C is compact, it must contain an accumulation point w of the w_i's. By continuity of g, this accumulation point satisfies $g(w) \geqslant a$. By continuity of 'dist', this point satisfies $\text{dist}(w, U) \geqslant \varepsilon$. This is a contradiction, since $w \in U$ by definition of U. □

Let $\boldsymbol{\sigma}(\mathbf{x}, t)$ be the continuum elastodynamic stress solution, where $\mathbf{x} \in \bar{\mathscr{B}}$ is the spatial coordinate and $t \in [0, t^*]$ is the time coordinate. Let us extend this solution to the interval $[0, t^* + \Delta t_1]$, where Δt_1 is the time-step for mesh $\mathscr{M}_1$ (which, without loss of generality, is assumed to be the largest among the Δt_i's). In this extension of $\boldsymbol{\sigma}$, we prevent crack nucleation by disabling the initiation criterion (so that the solution during $[t^*, t^* + \Delta t_1]$ continues to obey linear elasticity). It is assumed that this extension continues to be C^1 since crack formation was prevented.

By Lemma 1 (taking $C = \bar{\mathscr{B}} \times [0, t^*] \times \mathscr{A}$, $w = (\mathbf{x}, t, \theta)$, $g(w) = h(\boldsymbol{\sigma}(\mathbf{x}, t), \theta)$, $a = \sigma_c$ and $U = \{(\mathbf{x}^*, t^*, \theta^*)\}$), there exists a δ_1 such that the set of $(\mathbf{x}, t, \theta) \in \bar{\mathscr{B}} \times [0, t^*] \times \mathscr{A}$ satisfying $h(\boldsymbol{\sigma}(\mathbf{x}, t), \theta) \geqslant \sigma_c - \delta_1$ must also satisfy $\|\mathbf{x} - \mathbf{x}^*\| \leqslant \varepsilon$, $|t - t^*| \leqslant \varepsilon$ and $\text{dist}_{\mathscr{A}}(\theta, \theta^*) \leqslant \varepsilon$.

Since $\boldsymbol{\sigma}(\mathbf{x}, t)$ is C^1 on a compact set $\bar{\mathscr{B}} \times [0, t^* + \Delta t_1]$, there is a finite scalar L such that $\|\sigma(\mathbf{x}, t) - \sigma(\mathbf{x}', t')\| \leqslant L \max(\|\mathbf{x} - \mathbf{x}'\|, |t - t'|)$ for all $\mathbf{x}, \mathbf{x}' \in \bar{\mathscr{B}}$ and $t, t' \in [0, t^* + \Delta t_1]$. Similarly, since h is Lipschitz, for all 2×2 tensors $\boldsymbol{\sigma}, \boldsymbol{\sigma}'$ whose norms are bounded by the maximum stress occurring in the problem, and for all $\theta, \theta' \in \mathscr{A}$, $|h(\boldsymbol{\sigma}, \theta) - h(\boldsymbol{\sigma}', \theta')| \leqslant M \max(\|\boldsymbol{\sigma} - \boldsymbol{\sigma}'\|, \text{dist}_{\mathscr{A}}(\theta - \theta'))$, where M is a fixed scalar.

Next, let $p = \mathrm{d}h(\boldsymbol{\sigma}(\mathbf{x}, t), \theta)/\mathrm{d}t$ evaluated at $(\mathbf{x}^*, t^*, \theta^*)$. By the assumption made in Section 4, $p > 0$.

Choose $\eta > 0$ sufficiently small so that $\eta LM \leqslant \delta_1/4$, $p\eta \leqslant \delta_1$, and $\eta \leqslant \varepsilon$. Then for any $t \in [t^*, t^* + \eta]$, $\mathbf{x} \in \bar{\mathscr{B}}$ and $\theta \in \mathscr{A}$, $|h(\boldsymbol{\sigma}(\mathbf{x}, t), \theta) - h(\boldsymbol{\sigma}(\mathbf{x}, t^*), \theta)| \leqslant \delta_1/4$ (because the Lipschitz constant of σ is L and of h is M, and $\eta LM \leqslant \delta_1/4$). Consider a point $(\mathbf{x}, t, \theta) \in \bar{\mathscr{B}} \times [0, t^* + \eta] \times \mathscr{A}$ satisfying

$$h(\boldsymbol{\sigma}(\mathbf{x}, t), \theta) \geqslant \sigma_c - 0.75\delta_1 \tag{1}$$

If $t \geqslant t^*$, then by the inequality derived in this paragraph, $h(\boldsymbol{\sigma}(\mathbf{x}, t^*), \theta) \geqslant \sigma_c - \delta_1$, which is possible only if $\|\mathbf{x} - \mathbf{x}^*\| \leqslant \varepsilon$, $|t - t^*| \leqslant \eta \leqslant \varepsilon$, and $\text{dist}_{\mathscr{A}}(\theta, \theta^*) \leqslant \varepsilon$ by choice of δ_1. On the other hand, if $t < t^*$, then these same conclusions hold by the defining property of δ_1 (since $\sigma_c - 0.75\delta_1 > \sigma_c - \delta_1$).

The definition of p means that for $s > 0$, $h(\boldsymbol{\sigma}(\mathbf{x}^*, t^* + s), \theta^*) = \sigma_c + ps + O(s^2)$. By further decreasing η defined in the last paragraph (if necessary), we can assume that

$$h(\boldsymbol{\sigma}(\mathbf{x}^*, t^* + \eta), \theta^*) \geqslant \sigma_c + p\eta/2 \tag{2}$$

For each mesh $\mathscr{M}_i$, let $\boldsymbol{\sigma}_i(\mathbf{x}, t)$ be the finite-element approximation to $\boldsymbol{\sigma}(\mathbf{x}, t)$ computed using $\mathscr{M}_i$. In more detail, use the finite-element approximation to define $\boldsymbol{\sigma}_i$ spatially; if $\boldsymbol{\sigma}_i$ is discontinuous at element boundaries, then use any kind of averaging rule to also define $\boldsymbol{\sigma}_i$ on the boundaries. Use piecewise linear interpolation in time between discrete time-steps to make $\boldsymbol{\sigma}_i(\mathbf{x}, t)$ defined for all values of t. Let us now proceed with selecting I to satisfy the result. We accomplish this by stating several different requirements for I; the final I to select is the one that satisfies all the requirements (i.e. the maximum among the requirements).

Süli [38] has shown that the finite-element approximation will converge to the true linear elastic solution in the max-norm applied to the stress field under the assumptions made so far. This means that we can find an I sufficiently large so that for all $i \geqslant I$,

$$\|\boldsymbol{\sigma}(\mathbf{x}, t) - \boldsymbol{\sigma}_i(\mathbf{x}, t)\| \leqslant p\eta/(4M) \tag{3}$$

uniformly over $(\mathbf{x}, t) \in \bar{\mathscr{B}} \times [0, \min(t_i^*, t^* + \eta)]$, where t_i^* is the activation time of the first activated interface in the finite-element model based on $\mathscr{M}_i$.

Select I sufficiently large so that for all $i \geqslant I$, mesh $\mathscr{M}_i$ contains an interface edge e_i' whose midpoint $\mathbf{x}_i'$ satisfies $\|\mathbf{x}^* - \mathbf{x}_i'\| \leqslant p\eta/(4LM)$ and whose normal angle θ_i' satisfies $\text{dist}_{\mathscr{A}}(\theta^*, \theta_i') \leqslant p\eta/(2M)$. (For this step, we invoke Property P of the sequence of meshes.) Furthermore, assume I is sufficiently large so that the finite-element model defined on $\mathscr{M}_i$ possesses a discrete time-step t_i' satisfying $|t_i' - (t^* + \eta)| \leqslant p\eta/(4LM)$ (i.e. choose I sufficiently large so that $\Delta t_i \leqslant p\eta/(4LM)$ for all $i \geqslant I$).

Now we observe that the activation criterion in the discrete model is guaranteed to be satisfied for this edge e_i' at time-step t_i', unless it has satisfied earlier by a different edge (i.e. unless $t_i^* < t_i'$). This is because, assuming $t_i^* \geqslant t_i'$, we have $\|\mathbf{x}^* - \mathbf{x}_i'\| \leqslant p\eta/(4LM)$ and $|t^* + \eta - t_i'| \leqslant p\eta/(4LM)$ so $\|\boldsymbol{\sigma}(\mathbf{x}^*, t^* + \eta) - \boldsymbol{\sigma}(\mathbf{x}_i', t_i')\| \leqslant p\eta/(4M)$. Combining with (3) implies that $\|\boldsymbol{\sigma}(\mathbf{x}^*, t^* + \eta) - \boldsymbol{\sigma}_i(\mathbf{x}_i', t_i')\| \leqslant p\eta/(2M)$. Because h has Lipschitz-constant M, and by the assumption about θ_i' in the last paragraph, we conclude that $|h(\boldsymbol{\sigma}(\mathbf{x}^*, t^* + \eta), \theta^*) - h(\boldsymbol{\sigma}_i(\mathbf{x}_i', t_i'), \theta_i')| \leqslant p\eta/2$. By (2), this means $h(\boldsymbol{\sigma}_i(\mathbf{x}_i', t_i'), \theta_i') \geqslant \sigma_c$, i.e. the activation criterion will be satisfied at that interface at time t_i in the finite-element model.

Now, let e_i be the first activated interface in the model based on $\mathscr{M}_i$ (which could be equal to e_i' identified in the last paragraph). Suppose e_i is activated at time t_i, and let its midpoint and normal angle be $\mathbf{x}_i$ and θ_i, respectively. By definition of activation, we know that $h(\boldsymbol{\sigma}_i(\mathbf{x}_i, t_i), \theta_i) \geqslant \sigma_c$. Thanks to the existence of e_i', we are assured that $t_i \leqslant t^* + \eta$. Since $|\boldsymbol{\sigma}_i(\mathbf{x}_i, t_i) - \boldsymbol{\sigma}(\mathbf{x}_i, t_i)| \leqslant p\eta/(4M)$ by (3), then

$$|h(\boldsymbol{\sigma}(\mathbf{x}_i, t_i), \theta_i) - \underbrace{h(\boldsymbol{\sigma}_i(\mathbf{x}_i, t_i), \theta_i)}_{\geqslant \sigma_c}| \leqslant p\eta/4$$

which implies

$$h(\boldsymbol{\sigma}(\mathbf{x}_i, t_i), \theta_i) \geqslant \sigma_c - p\eta/4$$

We assumed earlier that η is sufficiently small so that $p\eta \leqslant \delta_1/4$, and thus

$$h(\boldsymbol{\sigma}(\mathbf{x}_i, t_i), \theta_i) \geqslant \sigma_c - \delta_1/4$$

This means that $\mathbf{x}_i, t_i, \theta_i$ satisfy hypothesis (1), and the outcome of that hypothesis is that $\|\mathbf{x}_i - \mathbf{x}^*\| \leqslant \varepsilon$, $|t_i - t^*| \leqslant \varepsilon$, and $\text{dist}_{\mathscr{A}}(\theta^*, \theta_i) \leqslant \varepsilon$. This concludes the proof of the main result.

6. A MESH REFINEMENT STUDY

In this section, we carry out a mesh refinement study, which is based on laboratory experiment, comparing pinwheel meshes to two other meshes. The set-up of the study is of the compact compression specimen (CCS) impact experiment used by Rittel and Maigre [39] and Maigre and Rittel [40]. The schematic of the experiment is shown in Figure 3. The PMMA specimen is fractured by impacting with a Hopkinson bar, and the load at the bar–specimen interface can be measured and subsequently used for the boundary condition of our simulations. We investigate, through a series of simulations, the effects of different mesh layouts on the crack path. This set-up is more interesting for a convergence study than the Kalthoff–Winkler experiment mentioned earlier because the crack path is not a straight line segment, and therefore there is no structured mesh that faithfully represents it.

Three mesh types—structured, unstructured, and pinwheel—are considered with two levels of refinement repeated for each of them. Our meshing procedure is as follows. First, a mesh is generated for a rectangle. In the case of the pinwheel family, this is accomplished by dividing the rectangle into subrectangles of aspect ratio $1:2$ and then using the Radin–Conway pinwheel tiling of two right-angle triangles that result from bisecting each subrectangle with a diagonal. The resulting tiling is turned into a mesh by splitting each triangle into three subtriangles as illustrated in Figure 2. In the case of the structured family, a standard cross-quadrilateral mesh is generated for the rectangle. In the case of the unstructured family, Shewchuk's Triangle mesh generator [41] is used to mesh a rectangle, with irregular (randomized) spacing of the nodes on the rectangle's boundary.

The meshes of the rectangle are then mapped to a subregion of the CCS geometry, namely, the crack-path zone illustrated in Figure 4, via a carefully chosen curvilinear coordinate transformation. This curvilinear transformation first maps the meshed rectangle into another rectangle of aspect ratio approximately $1:1.47$ using simple uniaxial dilation, and then maps the $1:1.47$ rectangle conformally into the crack-path zone using linear fractional transformations and an exponential map. This quantity (approximately 1.47) is the 'conformal modulus' of the crack-path zone [42]. The same conformal mapping is used in all experiments reported here. The resulting meshes of the crack-path zone are illustrated in Figure 5. The portion of the CCS geometry outside the crack-path zone is meshed by Triangle with an unstructured triangulation that matches the subdivision of the boundary of the crack-path zone mesh described earlier. The PINW program described earlier was not used for this study because two exterior boundaries of the CCS specimen are curves, while the current version of PINW can mesh only polygons.

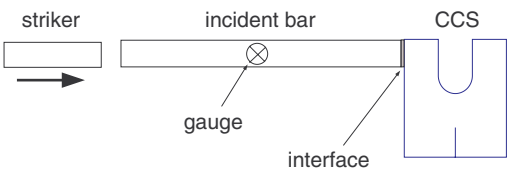

Figure 3. Schematic of CCS impact experiment. The dimensions of the specimen are 51 mm high, 46 mm wide, 11 mm deep. The notch at the bottom is 12 mm long, and the U-shaped notch is 15 mm wide and 27.5 mm high.

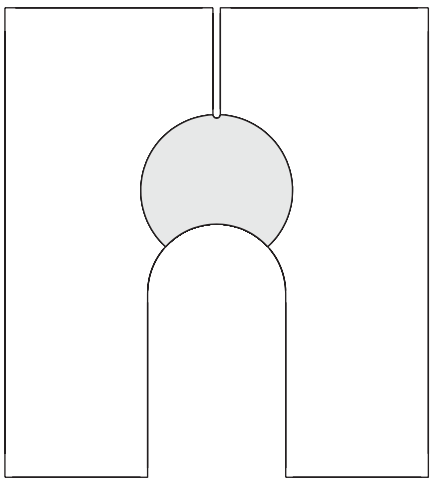

Figure 4. The crack-path zone is shaded in grey. Its boundary is composed of four circular arcs. This zone is meshed with a structured, unstructured or pinwheel mesh. The mesh is generated initially for a rectangle and then mapped to the crack-path zone via a composition of a uniaxial dilation followed by a conformal mapping. The region of the CCS geometry outside the crack-path zone is meshed using Shewchuk's Triangle.

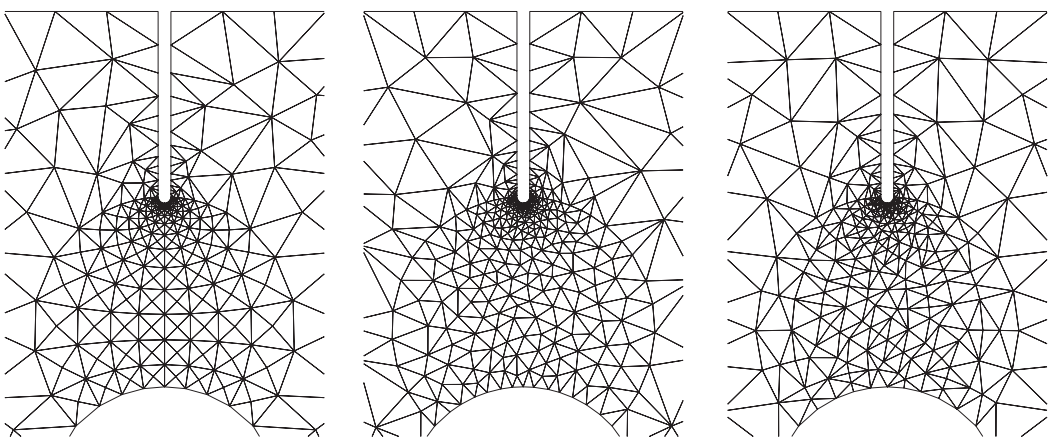

Figure 5. Examples of the three mesh families used for the crack-path zone: (a) structured; (b) unstructured; and (c) pinwheel.

Each of the three mesh types has two parameters that may be varied. The first parameter is the level of refinement. The second is the aspect ratio of the rectangle that is mapped to the crack-path zone. This second parameter affects the shape of the triangles in the final mesh. If a mesh family produces spatially convergent simulation results, then one expects that the

second parameter should have a diminishing effect on the crack path as the mesh is refined. In other words, suppose one has four distinct meshes M, N, M', N' of the same domain subject to the same loads such that the mesh sizes of M, N are both h and of M', N' are both h', where $h' \ll h$. The distinction between M and N depends on some other parameter (aspect ratio in this case), as does the distinction between M' and N'. For a convergent method, one expects the crack paths in M', N' to be closer to one another than are the two crack paths in M, N. This is because the crack paths in M', N' are each expected to be closer to the mathematical crack path compared to those in M, N. On the other hand, for a nonconvergent method, the dependence of the crack path on the mesh is not expected to decrease as the mesh size is reduced. Thus, by considering four meshes in this manner, we can check for convergence without having direct knowledge of the mathematical crack path.

Therefore, the methodology of our study is to consider the effect of varying the aspect-ratio parameter on each of two refinement levels for each of the three mesh families. Thus, this study involves a total of 18 meshes: for each of the three families, we used three aspect ratio values at the coarse level and three at the fine level. The actual mesh sizes ranged from 2800 to 5400 elements for the coarse meshes and from 12 000 to 21 000 elements for the fine meshes.

The initially rigid model cohesive model used in the experiments including the activation criterion are described in Reference [36]. The material parameters of the model are $\sigma_c = 105\,\text{MPa}$, $G_c = 0.0048\,\text{MPa m}$, $\beta = 1$. These parameters are, respectively, the critical normal traction that causes an interface element to activate, the fracture toughness, i.e. energy required to cause an interface to fail completely and become traction-free, and the mixity factor, which measures how shear and normal tractions are weighted in determining the effective opening displacement. Traction boundary conditions are used throughout; every surface is traction-free except for a boundary segment 12.7 mm long where the striker impacts. Along this segment, the traction is time-varying (although constant spatially along the length of the segment); the values of this traction were obtained from experimental measurements made at 260 equally spaced temporal points.

The results of the study are shown in Figures 6–8. It is evident from the figures that the aspect ratio parameter seemed to have a lesser effect on the fine pinwheel mesh than on the coarse pinwheel mesh, which is behaviour consistent with convergence. In other words, a visual inspection of the figure indicates that the crack paths in the fine mesh are more clustered together than the crack paths in the coarse mesh. We do not attempt to quantify this clustering because the convergence study in this example is not intended to be a rigorous effort to demonstrate convergence. Our rigorous analysis of Section 5 applies to crack initiation only.

In the structured mesh, on the other hand, the crack paths in the fine mesh do not appear to be any more closely clustered than those in the coarse mesh. In other words, changing the aspect ratio has a comparable effect at both refinement levels, a behaviour that is not consistent with convergence. In the case of the unstructured mesh, again varying the aspect ratio parameter seemed to have an almost equal effect on the fine and coarse meshes. For one of the values of the aspect-ratio parameter for the unstructured fine mesh, all the interfaces in a dense cloud were activated, so that a crack path is not even well defined. Other experiments we have carried out (not reported here) indicate that a reduction in the time-step can eliminate this cloud of activations. Because we did not see this anomalous behaviour in any of the other meshes of comparable size and because the time-step is already very small (50 times smaller than the elastodynamic CFL limit for this mesh), we did not attempt to vary the time-step for this single mesh.

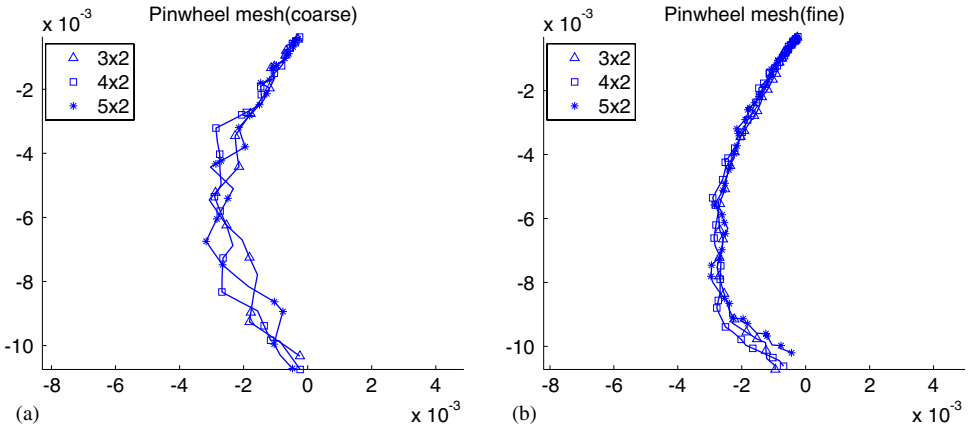

Figure 6. Crack path results on: (a) the coarse pinwheel mesh; and (b) the fine pinwheel mesh. The different paths shown in each plot correspond to different values of the second meshing parameter (aspect ratio).

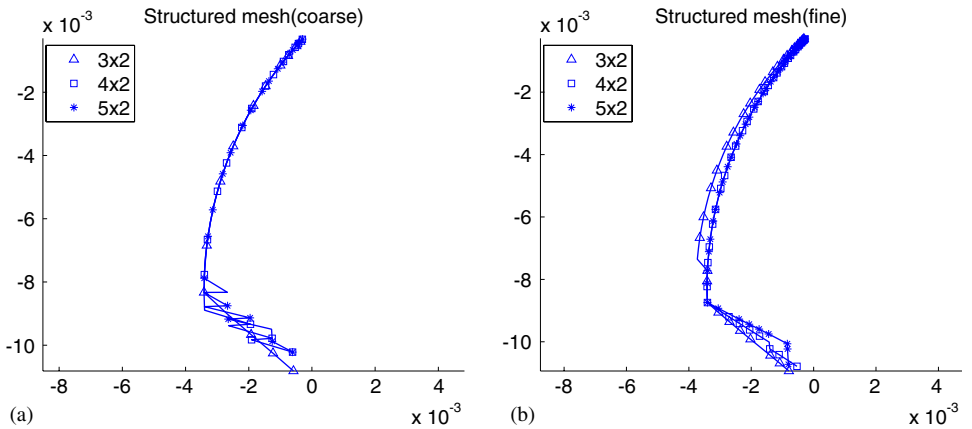

Figure 7. Crack path results on: (a) the coarse structured mesh; and (b) the fine structured mesh. The different paths shown in each plot correspond to different values of the second meshing parameter (aspect ratio).

Since our theory covers only the initiation of the crack (i.e. the first active interface), we also provide close-up views of the beginning of the crack for the unstructured and pinwheel families in Figures 9–10. In the case of the structured mesh, the initial portion of the crack is similar for both refinement levels and for all choices of the aspect ratio parameter for the artificial reason that in the structured mesh of the rectangular domain, the crack always initiates along one of the grid lines corresponding to vertical in the rectangular domain. This same grid line is present in all the mapped structured meshes. The pinwheel family seems to yield much more consistent crack patterns than unstructured, especially for the finer mesh.

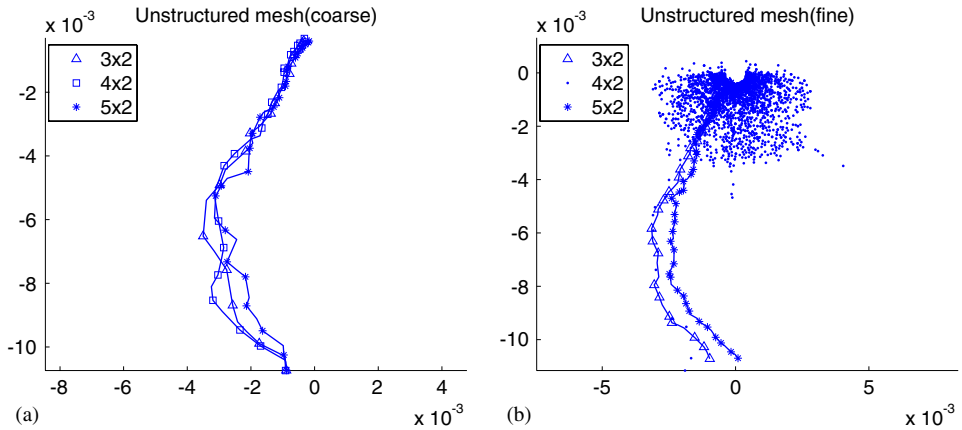

Figure 8. Crack path results on: (a) the coarse unstructured mesh; and (b) the fine unstructured mesh. The different paths shown in each plot correspond to different values of the second meshing parameter (aspect ratio).

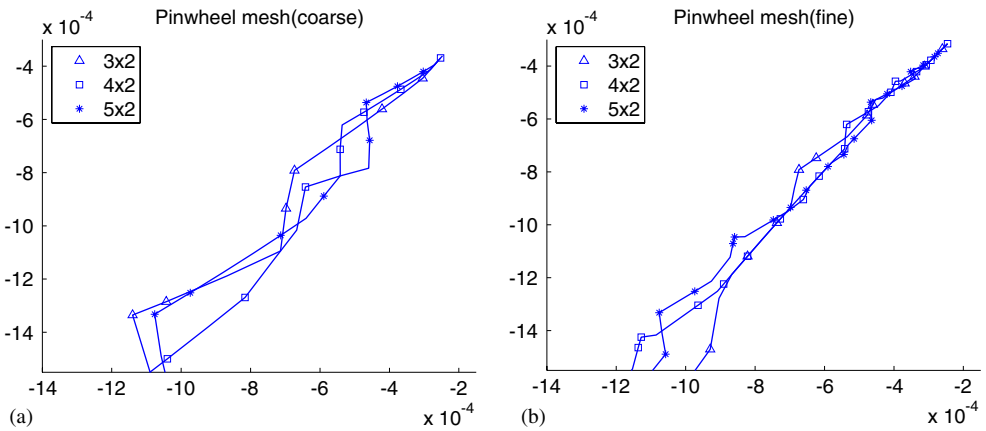

Figure 9. Close-up of the initial portion of the crack path on: (a) the coarse pinwheel mesh; and (b) the fine pinwheel mesh. The different paths shown in each plot correspond to different values of the second meshing parameter (aspect ratio).

The computational study presented in this section should not be interpreted as a computational 'proof' of the main theorem because only two refinement levels were considered. Rather, it should be understood as an indication that pinwheel meshes are an attractive choice for cohesive finite elements with moderate levels of refinement. A computational study intended to prove the main theorem would require an amount of computer time that is difficult to estimate but is expected to be very large. This is because the convergence rate of the main theorem is apparently slow. See further remarks on this matter in Section 7.

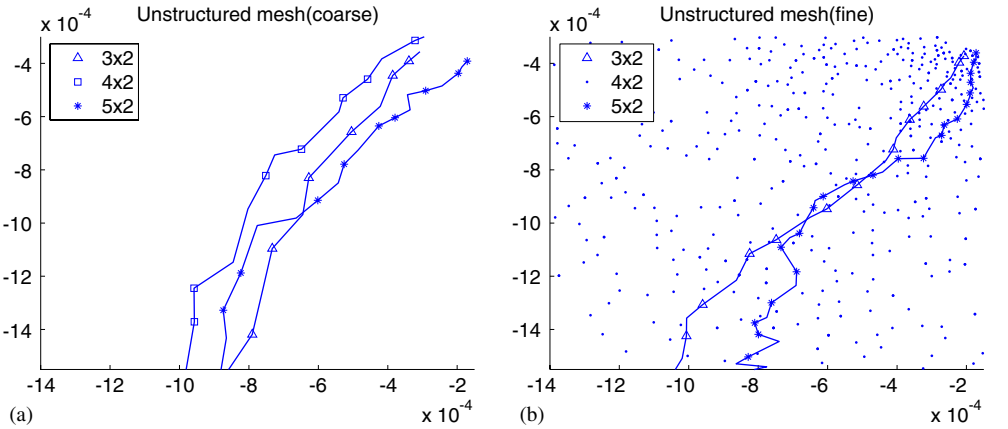

Figure 10. Close-up of the initial portion of the crack path on: (a) the coarse unstructured mesh; and (b) the fine unstructured mesh. The different paths shown in each plot correspond to different values of the second meshing parameter (aspect ratio).

7. CONCLUDING REMARKS

As mentioned in the introduction, this proof is the first spatial convergence proof of any kind for cohesive finite elements. It has, however, a number of limitations that perhaps could be resolved with further research.

One obvious limitation is that this result concerns only crack nucleation and not crack propagation. It seems quite difficult to extend the result to propagation for several reasons. First, there is no proof that the mathematical solution exists or is unique. Second, there is a limitation in pinwheel meshes that merits further discussion. As proved in Reference [35], pinwheel meshes have the property that any path is arbitrarily well approximated (in terms of its length) by a path in the mesh, as the mesh size tends to zero. Thus, the mathematical crack path could be well approximated in this purely geometric sense by a path in the pinwheel mesh. The proof of this approximation theorem, however, allows for an occasional edge in the approximation to be completely misaligned with the mathematical crack path. This occasional misalignment might be enough to cause the simulated crack path to diverge from the mathematical path in the setting of dynamics and fracture mechanics.

Another obvious limitation is that the result here covers only two dimensions. We expect that all the theory proposed here extends to three dimensions. The difficulty, however, is that there is no known mesh generator for three dimensions with Property P, i.e. no 3D version of PINW, even for very simple 3D geometries such as cubes.

A more subtle limitation is the assumption of smoothness of the stress field. This precludes the possibility of applying the result in the case that the crack initiates at a sharp notch in the domain. A moment's thought will convince the reader that this assumption is not merely a shortcoming of our proof technique but is rather a fundamental limitation of the theorem itself. If there were a sharp notch at the point of nucleation, then the choice of possible initial interface to activate is limited to the mesh edges emanating from that node, of which there are only a small constant number (e.g. five or six) regardless of the degree of refinement. Therefore,

the correct crack angle could not be captured in the limit of mesh refinement. In contrast, a smooth notch tip (such as the notch tip in the computational experiment of Section 6) has an infinite number of mesh edges emanating from it in the limit as the mesh size tends to zero.

A final limitation of the result here is that because the proof is primarily topological rather than analytical, no estimates of the convergence rate are forthcoming. We expect that the convergence rate in practice will be extremely poor (sublinear) because the convergence rate of Property P (i.e. how ε in the statement of Property P decreases as the mesh is refined) is known to be very slow. It would be interesting to come up with a convergence result like the one presented here but with a better convergence rate. Despite the expectation of a poor convergence rate, our computational experiment performed surprisingly well when compared to either a family of structured meshes or unstructured meshes. This hints that the computed answers may be close to the mathematical limits even when Property P is far from asymptotic convergence.

REFERENCES

1. Dugdale DS. Yielding of steel sheets containing slits. *Journal of the Mechanics and Physics of Solids* 1960; **8**:100–104.
2. Barenblatt GI. The mathematical theory of equilibrium of cracks in brittle fracture. *Advances in Applied Mechanics* 1962; **7**:55–129.
3. Rice JR. A path independent integral and the approximate analysis of strain concentration by notches and cracks. *ASME Journal of Applied Mechanics* 1968; **35**:379–386.
4. Rahul-Kumar P, Jagota A, Bennison SJ, Saigal S, Muralidhar S. Polymer interfacial fracture simulations using cohesive elements. *Acta Materialia* 1999; **47**(15–16):4161–4169.
5. Shabrov MN, Needleman A. An analysis of inclusion morphology effects on void nucleation. *Modelling and Simulation in Materials Science and Engineering* 2002; **10**:163–183.
6. Tvergaard V. Effect of fibre debonding in a whisker-reinforced material. *Material Science and Engineering* 1990; **A125**:203–213.
7. Rosakis AJ, Samudrala O, Singh RP, Shukla A. Intersonic crack propagation in bimaterials. *Journal of the Mechanics and Physics of Solids* 1998; **46**:1789–1813.
8. Siegmund T, Needleman A. A numerical study of dynamic crack growth in elastic–viscoplastic solids. *International Journal of Solids and Structures* 1997; **34**(7):769–787.
9. Alfano G, Crisfield MA. Finite element interface models for the delamination analysis of laminated composites: mechanical and computational issues. *International Journal for Numerical Methods in Engineering* 2001; **50**:1701–1736.
10. Han TS, Ural A, Chen CS, Zehnder AT, Ingraffea AR, Billington SL. Delamination buckling and propagation analysis of honeycomb panels using a cohesive element approach. *International Journal of Fracture* 2002; **115**(2):101–123.
11. Dwivedi SK, Espinosa HD. Modeling dynamic crack propagation in fiber-reinforced composites including frictional effects. *Mechanics of Materials* 2003; **35**:481–509.
12. Espinosa HD, Zavattieri PD. A grain level model for the study of failure initiation and evolution in polycrystalline brittle materials. Part I: theory and numerical implementation. *Mechanics of Materials* 2003; **35**:333–364.
13. Espinosa HD, Zavattieri PD. A grain level model for the study of failure initiation and evolution in polycrystalline brittle materials. Part II: numerical examples. *Mechanics of Materials* 2003; **35**:365–394.
14. Zavattieri PD, Espinosa HD. Grain level analysis of crack initiation and propagation in brittle materials. *Acta Materialia* 2001; **49**:4291–4311.
15. Needleman A. A continuum model for void nucleation by inclusion debonding. *Journal of Applied Mechanics* 1987; **38**:289–324.
16. Xu XP, Needleman A. Numerical simulations of fast crack growth in brittle solids. *Journal of the Mechanics and Physics of Solids* 1994; **42**(9):1397–1434.

17. Camacho GT, Ortiz M. Computational modeling of impact damage in brittle materials. *International Journal of Solids and Structures* 1996; **33**(22–29):2899–2938.
18. Miller O, Freund LB, Needleman A. Modeling and simulation of dynamic fragmentation in brittle materials. *International Journal of Fracture* 1999; **96**:101–125.
19. Repetto EA, Radovitzky R, Ortiz M. Finite element simulation of dynamic fracture and fragmentation of glass rods. *Computer Methods in Applied Mechanics and Engineering* 2000; **183**(1–2):3–14.
20. Zhai J, Zhou M. Finite element analysis of micromechanical failure mode in heterogeneous brittle solids. *International Journal of Fracture* (*special issue on Failure Mode Transition*) 1999; 161–180.
21. Bittencourt T, Ingraffea AR, Llorca J. Simulation of arbitrary, cohesive crack propagation. In *Fracture Mechanics of Concrete Structures*, Bazant Z (ed.). Elsevier Applied Science: New York, 1992; 339–350.
22. Moës N, Dolbow J, Belytschko T. A finite element method for crack growth without remeshing. *International Journal for Numerical Methods in Engineering* 1999; **46**:131–150.
23. Pandolfi A, Krysl P, Ortiz M. Finite element simulation of ring expansion and fragmentation. *International Journal of Fracture* 1999; **95**:279–297.
24. Klein P, Foulk J, Chen E, Wimmer S, Gao H. Physics-based modeling of brittle fracture: cohesive formulations and the application of meshfree methods. *Technical Report SAND2001-8099*, Sandia National Laboratories, December 2000.
25. Papoulia KD, Sam C-H, Vavasis SA. Time continuity in cohesive finite element modeling. *International Journal for Numerical Methods in Engineering* 2003; **58**(5):679–701.
26. Kubair DV, Geubelle PH. Comparative analysis of extrinsic and intrinsic cohesive models of dynamic fracture. *International Journal of Solids and Structures* 2003; **40**(15):3853–3868.
27. Remmers JJC, de Borst R, Needleman A. A cohesive segments method for the simulation of crack growth. *Computational Mechanics* 2003; **31**:69–77.
28. Rabczuk T, Belytschko T. Cracking particles: a simplified meshfree method for arbitrary evolving cracks. *International Journal for Numerical Methods in Engineering* 2004; **61**:2316–2343.
29. Belytschko T, Chen H, Xu J, Zi G. Dynamic crack propagation based on loss of hyperbolicity and a new discontinuous enrichment. *International Journal for Numerical Methods in Engineering* 2003; **58**:1873–1905.
30. C-H Sam. A robust formulation and solution of initially rigid cohesive interface models. *Ph.D. Thesis*, Cornell University, 2005.
31. Kalthoff JF, Winkler S. Failure mode transition at high rates of shear loading. *International Conference on Impact Loading and Dynamic Behavior of Materials*, vol. 1, 1987; 185–195.
32. Zhang Z, Paulino GH. Cohesive zone modeling of dynamic failure in homogeneous and functionally graded materials. *International Journal of Plasticity* 2005; **21**:1195–1254.
33. Radin C. The pinwheel tilings of the plane. *The Annals of Mathematics* 1994; **139**(3):661–702.
34. Radin C, Sadun L. The isoperimetric problem for pinwheel tilings. *Communications in Mathematical Physics* 1996; **177**:255–263.
35. Ganguly P, Vavasis SA, Papoulia KD. An algorithm for two-dimensional mesh generation based on the pinwheel tiling. *SIAM Journal on Scientific Computing* 2004, submitted.
36. Sam C-H, Papoulia KD. Obtaining initially rigid cohesive finite element models that are temporally convergent. *Engineering Fracture Mechanics* 2005, in press.
37. LeVeque RJ. *Numerical Methods for Conservation Laws*. Birkhauser: Basel, 1990.
38. Süli E. Private communication, 2005.
39. Rittel D, Maigre H. A study of mixed-mode dynamic crack initiation in PMMA. *Mechanics Research Communications* 1996; **23**(5):475–481.
40. Maigre H, Rittel D. Mixed-mode quantification for dynamic fracture initiation: application to the compact compression specimen. *International Journal of Solids and Structures* 1993; **30**(23):3233–3244.
41. Shewchuk JR. A two-dimensional quality mesh generator and Delaunay triangulator. *Technical Report*, Computer Science Division, University of California, Berkeley, 2002.
42. Ahlfors LV. *Complex Analysis*: *An Introduction to the Theory of Analytic Functions of One Complex Variable*. McGraw-Hill: New York, 1979.

